

Heat-treatment effect on the nanosized graphite π -electron system during diamond to graphite conversion

B. L. V. Prasad, Hirohiko Sato, and Toshiaki Enoki*

Department of Chemistry, Tokyo Institute of Technology, 2-12-1 Ookayama, Meguro-ku, Tokyo 152-8551, Japan

Yoshihiro Hishiyama and Yutaka Kaburagi

Faculty of Engineering, Musashi Institute of Technology, 1-28-1, Tamazutsumi, Setagaya-ku, Tokyo 158-8557, Japan

A. M. Rao and P. C. Eklund[†]

Department of Physics and Astronomy and Center for Applied Energy Research, University of Kentucky, Lexington, Kentucky 40506

Kyoichi Oshida

Nagano National College of Technology, 716 Tokuma, Nagano 381-8550, Japan

Morinobu Endo

Department of Electrical Engineering, Shinshu University, Nagano 380-8553, Japan

(Received 10 April 2000; revised manuscript received 15 June 2000)

Graphite nanoparticles were prepared by the heat treatment of diamond nanoparticles in the range 900–1600 °C. X-ray diffraction, transmission electron microscopy (TEM) and Raman scattering studies indicate that the onset temperature of the diamond-graphite transition is around 1200 °C and the complete conversion of diamond to graphite occurs at 1600 °C. Based on the structural characteristics the samples are categorized into sp^3 -dominated (as-prepared and 900 °C), sp^2 : sp^3 mixed-phase (1200 and 1400 °C), and sp^2 -dominated systems (1600 °C). The larger c -axis repeat distances and the high-resolution TEM images for the sp^2 : sp^3 mixed-phase systems denote the presence of the remnant buckling feature of the diamond (111) planes in the graphene sheets. Magnetic susceptibility and ESR studies suggest the development of itinerant- π -electron system from the 1200 °C and higher-temperature heat-treated samples. The completely graphitized sample reveals the important role of edge-inherited nonbonding π -electron states in the electronic structure. The Raman G -peak position and the orbital diamagnetism show considerable deviation from the bulk-graphite values, which is explained on the basis of charge transfer from the graphite π band to the localized edge states and the resulting shifting of the Fermi level. The enhanced spin-lattice relaxation rates in the case of more graphitized samples heat-treated at 1400 and 1600 °C are expected to arise from the involvement of the localized edge-state electrons. In the less-graphitized 1200 °C heat-treated sample, however, the corrugated nature of the graphene planes is likely to hinder such fast-relaxation processes.

I. INTRODUCTION

The electronic properties of nanoscale materials are mainly controlled by the quantum size effect,¹ which causes a splitting in the electron-energy spectrum, and the surface effects. Carbon-based nanomaterials such as fullerenes, nanotubes, and nanographites^{2–4} have been attracting greater attention these days because of their novel electronic properties stemming from their specific sizes. Among these carbon-based materials fullerenes and nanotubes have closed surfaces due to the participation of pentagon rings.² On the other hand, nanographites are characterized by the stacking of finite flat graphene sheets having open edges. It has been pointed out that the electronic properties of nanographites are greatly influenced by their edge shapes apart from quantum size effects and surface effects. An arbitrarily shaped graphene sheet comprises two kinds of edges; zigzag type and armchair type, where the former has a *trans*-polyacetylene type structure, while the later has a *cis*-polyacetylene type. In the case of a hypothetical graphene sheet having only zigzag edges, theoretical calculations by

Fujita and co-workers^{5–7} suggested that nonbonding π levels superimposed on the bonding π and antibonding π^* bands appear around the Fermi energy due to the specific topology of the zigzag edges. No abnormality of this kind was found in the case of a graphene sheet composed of only armchair edges. However, in a general finite graphene sheet consisting of both types of edges, even a few zigzag sites per sequence are shown to lead to non-negligible edge-state effects, resulting in an enhancement in the electronic density of states around the Fermi energy.

According to previous works with ultradisperse diamond (UDD) clusters, heat-treated diamond nanoparticles are a good model system of nanographite. UDD clusters prepared by explosion-induced techniques have an extremely small distribution of sizes with most of the particles having dimensions of 4–5 nm.⁸ The as-prepared diamond nanoclusters are known to be covered by functional groups on the surfaces, and heat treatment easily reconstructs the diamond (111) planes into graphite (001) planes after stripping off the functional groups.^{8–10} From earlier reports^{11–15} the diamond-graphite conversion is complete at about 1600 °C. The pre-

pared graphite nanoparticles (size $\sim 7\text{--}8$ nm) form a polyhedron with a hollow inside. The faces of the polyhedron comprise a stacking of 3–7 graphene sheets with an in-plane size of 3–4 nm and an intersheet distance of 0.353 nm. The larger intersheet distance compared to graphite (0.3345 nm) and the disordered stacking feature suggest a considerable reduction in the weak interlayer interaction, so that the graphite nanoparticles can be treated as an assembly of very weakly bound graphene nanosheets. Magnetic susceptibility studies indicated a considerable enhancement in the density of states supporting the theoretical suggestion that edge-inherited nonbonding π levels appear around the Fermi energy.¹¹

Here, it would be interesting to investigate how the specially featured π -electron nanosystem develops during the heat-treatment-induced diamond-to-graphite conversion. In this connection, several reports have appeared on the structural transformations of UDD particles annealed at various temperatures.^{11,13–15} However, no report has been published so far on the study of the gradual change of electronic properties as a function of heat-treatment temperature during the diamond-graphite transformation of these nanoparticles. In this paper we report our results on the structural and electronic properties of the diamond nanoparticles heat-treated in the temperature range 900–1600 °C. This study was carried out to understand the correlation between the change in the structure and electronic properties during the diamond-graphite phase transition, with special attention paid to the role of nonbonding edge states.

II. EXPERIMENTAL DETAILS

Graphite nanoparticles were prepared by the graphitization of diamond-nanoparticle powder [Cluster Diamond, Tokyo Diamond Tools Mfg. Co. Ltd. (grain size 4–6 nm)] in an inert argon atmosphere. Judging from the characterization with transmission electron microscopy, the mean size and the size distribution of the diamond particles were in good agreement with those reported (catalog specifications). In order to avoid contamination with magnetic impurities, we boiled diamond nanoparticles in concentrated HCl before use. By this treatment we could remove traces of the transition-metal magnetic impurities present in the as-prepared diamond nanoclusters (as evidenced by the absence of residual magnetization at $H=0$ T and $T=5.0$ K). 20–50 mg of the acid-treated pristine diamond-nanoparticle powder placed in a graphite crucible was heat-treated in a graphite furnace in an argon atmosphere. To investigate the temperature dependence of the graphitization process, we employed 900, 1200, 1400, and 1600 °C for heat-treatment temperatures (HTT's). In this paper the samples are abbreviated as HTT900, HTT1200, etc., where the digits denote the heat-treatment temperature employed, in °C. The holding time at the peak temperature was 3 h. The structure of the obtained particles was characterized by means of high-resolution transmission electron microscopy (HRTEM), x-ray powder diffraction, and Raman scattering. Transmission electron microscope observation was carried out using a JEOL JEM2010 instrument with an acceleration voltage of 200 kV. X-ray diffraction profiles were obtained by a Rigaku RINT-2400 instrument with a Cu target (50 kV, 120 mA). The peak positions were

calibrated using Si powder as standard. Raman spectra were measured in the backscattering configuration using 514.5-nm Ar laser excitation. The scattered light was analyzed in a Jobin-Yvon HR460 single-grating spectrometer equipped with a charge-coupled array detector and a holographic notch filter (Kaiser Optical Systems, Inc., Ann Arbor, MI). The samples were pressed into pellets by mixing with 10% of KBr by weight, since these powders did not make good pellets by themselves. To avoid laser damage to the sample the experiments were conducted at low laser powers (2 W/cm²). Electronic and magnetic properties were investigated by means of ESR and magnetic susceptibility. ESR spectra were measured with a conventional X-band spectrometer (JEOL JES-TE20) in the temperature range 2–300 K, where the magnetic field and microwave frequency were calibrated using an NMR gaussmeter and a frequency counter, respectively. The samples were put at the bottom of a quartz glass tube and were heat-treated to about 350 °C under vacuum for about 2 h and then sealed. To obtain the g values correctly, we used DPPH (diphenyl picrylhydrazyl) as an internal standard. The precision of the g value is better than ± 0.0001 . ESR intensities and spin-lattice relaxation times were calibrated using DPPH as a reference. ESR saturation curves were taken up to the maximum microwave power of 200 mW for the estimation of spin-lattice relaxation times. The magnetic susceptibility and magnetization were measured with a Quantum Design MPMS-5 superconducting quantum-interference device (SQUID) susceptometer in the temperature range 2–300 K under magnetic fields up to 5 T. The samples were prepared using similar procedures that were adopted for the preparation of ESR samples.

III. RESULTS

Figure 1 provides the HRTEM pictures of the diamond nanoparticles heat-treated at various temperatures. The gradual changes in the structures of diamond nanoparticles are clearly seen and are qualitatively very similar to the earlier reports.¹⁴ The elemental analysis of the as-prepared sample roughly breaks down to (in mol %) 85% of carbon, 9.7% of oxygen, 2.5% nitrogen, and 2.5% hydrogen (catalog specifications). The diamond nanoparticles appear brownish to the naked eye, suggesting that the surface is covered by functional groups, and the TEM image of the pristine diamond nanoparticles shows a disordered surface structure as expected. However, the magnified image clearly reveals lattice fringes observed from the diamond (111) planes [inset, Fig. 1(a)]. Heat treatment at 900 °C induces a noticeable change in the physical appearance of the particles with a clear change of color to black from the brownish appearance of pristine diamond particles. The HRTEM image at this heat-treatment temperature, however, still shows large portions of unconverted diamond, while the surface seems to have been covered with portions of amorphous carbon with no clear long-range order present [inset, Fig. 1(b)]. As the heat treatment is increased, the TEM images reveal the formation of several small graphitic islands at 1200 °C and then an increase in in-plane as well as interplane ordering of these small graphitic islands at 1400 °C. However, the magnified images still display the diamond (111) lattice images, implying the presence of a diamond core. At 1600 °C, the diamond is completely converted to graphite, since the diamond (111) lattice images are absent even in the magnified image [Fig.

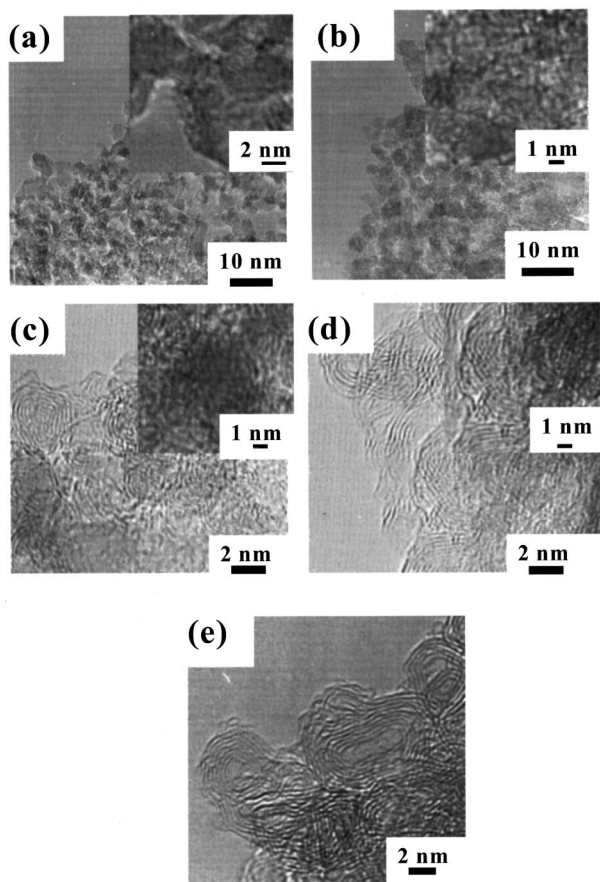


FIG. 1. The HRTEM images of the (a) as-prepared, (b) HTT900, (c) HTT1200, (d) HTT1400, and (e) HTT1600 samples. The insets show the magnified images of these samples, clearly revealing the presence of diamond (111) lattice images in case of as-prepared, HTT900, HTT1200, and HTT1400 samples. Different scales were used to highlight the salient features of the samples.

1(e)]. The formed graphite nanoparticles have a polyhedral shape with a hollow inside. The size of the particle is about 7–8 nm.

Figure 2 depicts the x-ray diffractograms of the 900, 1200, 1400, and 1600 °C heat-treated samples along with the diffractogram of the non-heat-treated pristine diamond nanoparticles. The structural transformation from diamond to graphite is very clear and is in good agreement with the TEM studies. The salient features are a peak centered around 43° corresponding to diffraction from the diamond (111) planes in the diamond nanoparticles and a peak at 26° for the HTT1600 sample. The as-prepared and HTT900 samples display a peak only at 43°, suggesting the absence of graphite phase, but for the HTT1200 and HTT1400 samples peaks both from the diamond (111) planes and graphite (002) are clearly visible, indicating the coexistence of diamond and graphite phases. In the x-ray diffraction pattern of the HTT1600 sample, the peak from diamond (111) planes is absent, judging from the slight increase in the peak position and the asymmetric peak shapes; instead new peaks that could be assigned to graphite (100) and (101) appear around 45°. This clearly shows that at 1600 °C all the diamond particles are completely converted to graphite, in agreement with the HRTEM results.

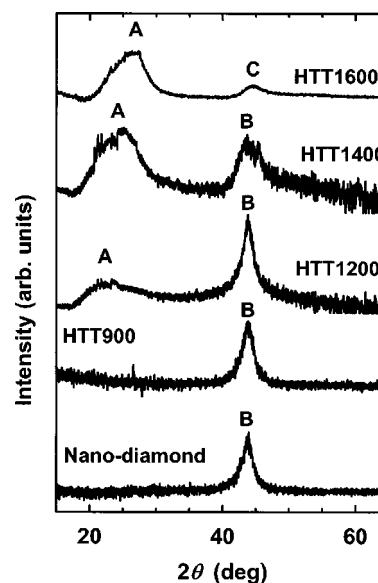


FIG. 2. Observed x-ray profiles for diamond nanoparticles, HTT900, HTT1200, HTT1400, and HTT1600 samples. For clarity the profiles are shifted vertically. A, B, and C are diffraction peaks indexed to graphite (002), diamond (111), and graphite (100) and (101), respectively.

After correcting for the Lorentz polarization factor and the atomic scattering factor,¹¹ the intensities of the graphite (002) and the diamond (111) peaks were fitted to Lorentzian functions. Comparing the intensities of these peaks, the conversion ratio of diamond to graphite was determined at each HTT. (We would like to make it clear that the graphite fraction only reflects the ordering along the *c* axis and should not be taken as an indication of the absolute *sp*²:*sp*³ carbon ratio of these samples.) The observed graphite *c*-axis repeat distances l_c [from the graphite (002) peak position], the size of diamond particles, L_D [from the diamond (111) peak width], the conversion factors, and the thickness of graphite crystallites, l_c [from the graphite (002) peak width] along with the graphite in-plane domain sizes, L_a [obtained from the graphite (100) peak and Raman studies] are all provided in Fig. 3. While the l_c and L_D decrease with HTT, the l_c , L_a , and graphite fraction increase with the HTT, indicating a gradual development of graphite phase at the expense of the diamond phase from the surface inwards.

The Raman features of these samples are very similar to other disordered carbons and the heat-treated ultradisperse diamond particles already available in literature.^{13,14} The main features observed in the Raman spectra of our samples are a peak around 1350 cm^{-1} , corresponding to the disorder-induced line (*D* peak) and another peak around 1560–1590 cm^{-1} corresponding to the Raman-allowed E_{2g_2} mode (*G* peak) in graphite.¹⁶ A weak shoulder also ascribed to the disorderiness of graphite¹⁶ is found for all the samples around 1620 cm^{-1} . For the HTT900 and HTT1200 samples, however, we found additional scattering intensity between the 1350- and 1580- cm^{-1} peaks. Though such additional peaks were observed in some earlier studies based on disordered carbon-based materials,^{17,18} the origin of these peaks is not very clear yet and they are generally assigned to the features in the density of vibrational states between 1350 and 1590

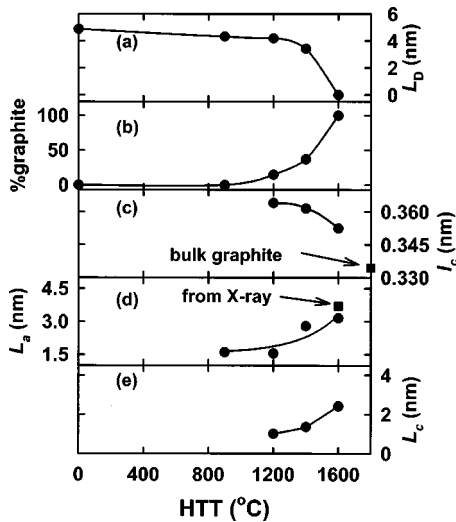


FIG. 3. The variation of the structural parameters with HTT. (a) The diamond size (L_D), (b) the conversion ratio of diamond to graphite, (c) the observed graphite c -axis repeat distance (I_c), (d) the graphite in-plane domain size (L_a), and (e) the graphite thickness along the c axis (L_c). The solid lines are only guides for the eye. (See text for the details of the analysis carried out to obtain these values.)

cm^{-1} associated with very small crystallite size effects.¹⁷ In these disordered graphitic systems the ratio of the integrated intensity of the G peak to the integrated intensity of the D peak is known to provide the average graphite in-plane domain size (L_a) in nm by the equation,¹⁹

$$L_a = 4.4 \frac{I_G}{I_D},$$

when an excitation wavelength of 514.5 nm is used. The calculated in-plane domain sizes (L_a) for various HTT's are also provided in Fig. 3(d), which shows an increase with heat treatment.

Magnetic susceptibility studies were carried out to get insight into the magnetic and electronic properties of these materials. The magnetization curve with respect to field shows no residual magnetization at $H=0$ T and $T=5.0$ K, supporting the contention that these materials are devoid of any transition-metal ferromagnetic impurities. The absence of magnetic impurities is further confirmed by the magnetization curves well fitted to the $S=\frac{1}{2}$ Brillouin curve and the small ESR linewidths and g -value deviations, which are presented later. The observed magnetization curve at $T=5.0$ K could be explained as a sum of a field-dependent linear term with a negative slope, and a Brillouin-curve-type positive term. The linear term constitutes core and orbital diamagnetic terms and a Pauli paramagnetic term, while the Brillouin-type term originates from the localized spins of $S=\frac{1}{2}$. The temperature dependence of magnetic susceptibility is given in Fig. 4 for these samples. The susceptibility at 300 K is negative for all the samples, which becomes positive (except for HTT1600 sample) and shows a Curie-like behavior at low temperatures. The susceptibility at infinite temperature χ_0 is obtained by plotting χ vs $1/T$ and then extrapolating the χ value to $1/T=0$. The obtained χ_0 is plotted against HTT in Fig. 5(a). The value is negative for all the

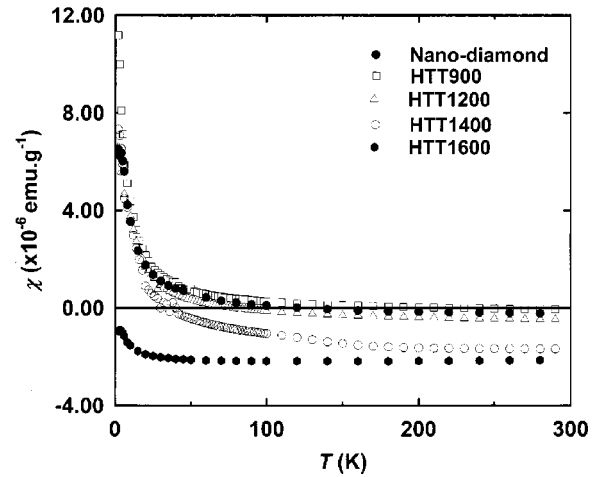


FIG. 4. The magnetic susceptibility as a function of temperature for the diamond nanoparticles, HTT900, HTT1200, HTT1400, and HTT1600 samples under a magnetic field of $H=1$ T.

samples and shows an increase in the absolute value as the HTT increases. The observed χ_0 is -0.38×10^{-6} emu/g for diamond-nanoparticle sample. There is not much change when the sample is heat-treated to 900 °C, but when the HTT is raised to 1200 °C χ_0 becomes -0.66×10^{-6} emu/g. The absolute value of χ_0 increases further as the HTT is raised and reaches a value of -2.22×10^{-6} emu/g for the HTT1600 sample, which is about 30% of that observed for bulk graphite. The increment in the absolute value of χ_0 originates from the gradual development of π -electron network, which is discussed in detail later. After subtracting the term χ_0 from the observed susceptibility, the temperature dependence of the susceptibility could be fitted well to the Curie-Weiss law $C/(T-\Theta)$, except for the HTT1600 sample, where C and Θ are the Curie and Weiss constants, respectively. The localized spin density of each sample could be estimated from the Curie constant. In the HTT1600 sample, the temperature dependence of the susceptibility has contributions from the orbital susceptibility χ_{orb} in addition to the Curie-Weiss term. In this case, the Curie-Weiss term is obtained after subtract-

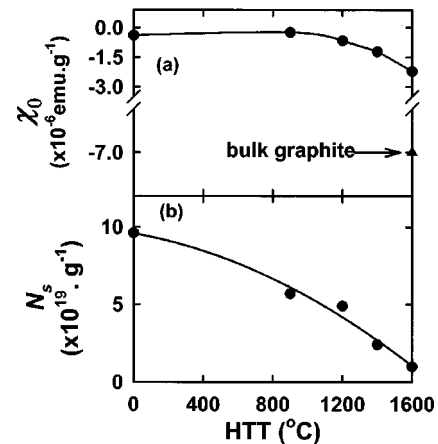


FIG. 5. (a) The constant term in the susceptibility, χ_0 [$=\chi(T \rightarrow \infty)$] and (b) the localized spin concentration N_s as a function of HTT. The value of the χ_0 of bulk graphite is also shown, which is the orientational average value.

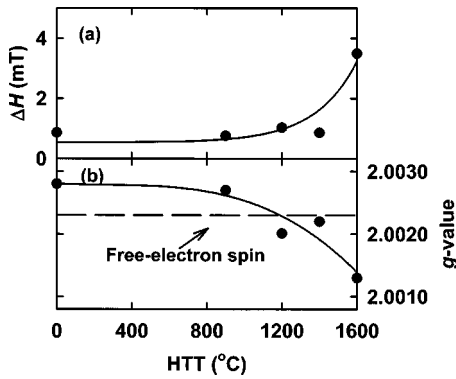


FIG. 6. (a) The observed ESR linewidths and (b) g values as a function of HTT (the data for the HTT1600 sample are for broad signal). The precision of Δg is better than ± 0.0001 . The solid lines are only guides for the eye.

ing χ_{orb} , which is estimated¹¹ by fitting the temperature dependence of the susceptibility with the Kotosonov equation²⁰ for disordered graphite. The Weiss constants obtained were generally negative and very small or negligible (-5 to 0 K), suggesting a very weak antiferromagnetic or negligible interaction among these localized spins. The number of spins calculated from the Curie constants, N_s , is estimated at $9.6 \times 10^{19}/\text{g}$ for the non-heat-treated nanoparticle diamond. It shows a decreasing trend with the HTT, finally reaching a value of $0.99 \times 10^{19}/\text{g}$ at 1600°C and is plotted in Fig. 5(b).

ESR investigations revealed a single Lorentzian line shape for the nanoparticle diamond, HTT900, HTT1200, and HTT1400 samples. However, the HTT1600 sample depicts two lines; a broad signal (peak-to-peak linewidth $\Delta H = 3.5$ mT) and a narrow signal ($\Delta H = 0.4$ – 0.5 mT).¹¹ In compliance with the magnetic susceptibility studies, the broad signal is ascribed to the π electrons giving rise to the Pauli susceptibility, while the narrow signal comes from the localized Curie spins.¹¹ The coexistence of the two signals implies that there is no appreciable interaction between these two spins in the HTT1600 sample. Figure 6 provides the dependence of the linewidth ΔH and the g value observed at room temperature as a function of the HTT. The linewidths are in the range of about 1 mT for the samples heat-treated below 1600°C , which jumps to a value of about 3.5 mT (broad signal) for the HTT1600 sample [Fig. 6(a)]. The g value for the nanoparticle diamond is about 2.0028, which is in good agreement with the reported value of 2.0029 for microcrystalline diamond powders prepared from mechanical grinding of bulk diamond crystals.²¹ The g value gradually decreases as the HTT is increased [Fig. 6(b)] and reaches a value of 2.0013 for the HTT1600 sample. The narrow linewidths and g values close to the free-electron g value show that the spins originate from carbon-inherited species but not from transition-metal impurities, indicating the effectiveness of acid treatment for removing these magnetic impurities. No appreciable temperature dependence of g values or linewidths was observed for the nanoparticle diamond, HTT900, HTT1200, and HTT1400 samples, while it becomes very difficult to determine the g value of the HTT1600 sample at low temperatures because of the overlap of two signals.

The spin-lattice relaxation times at room temperature

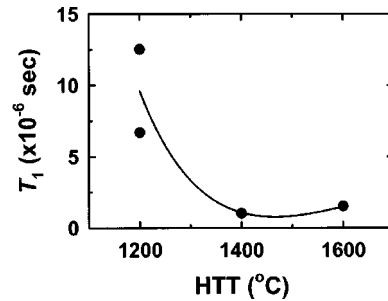


FIG. 7. The spin-lattice relaxation times at room temperature as a function of the HTT (the two points at 1200°C were obtained from different samples prepared in different batches). The solid line is only a guide for the eye.

were determined by analyzing the power saturation effects of the ESR signals.²² The observed T_1 shows interesting transformations as the HTT is increased. Actually, the T_1 value is estimated at $(0.7$ – $1.2) \times 10^{-5}$ sec for 1200°C using samples prepared in different batches. It decreases almost by an order of magnitude to about $(1.0$ – $1.5) \times 10^{-6}$ sec for the HTT1400 and HTT1600 samples as shown in Fig. 7. This phenomenon is proposed to originate from the structural changes associated with the increase in HTT (*vide infra*).

IV. DISCUSSION

A. Structural characteristics

The detailed structural features of these heat-treated diamond particles and the structural transformation from the diamond to graphite are well documented in the literature,^{13–15} and here we only provide a brief overview pertinent to our discussion on the transformation of electronic properties. As mentioned earlier, the σ dangling bonds protruding from diamond surfaces are unstable at room temperature and are easily attacked by oxygen and hydrogen present in the atmosphere resulting in surfaces covered by functional groups.^{9,10} Heat treatment at about 800°C strips these functional groups, creating defects, and a further rise in the HTT converts the puckered diamond (111) planes to planar graphite (001) planes, with the nucleation of diamond-graphite phase taking place at the defect centers.^{9,10} In the initial stages of the heat treatment very, very small graphitic islands are formed on the surface of the diamond nanoparticles and the c -axis repeat distance observed for these low-temperature heat-treated samples is generally larger than that of bulk graphite (Fig. 3). The larger c -axis repeat distances at these low HTT's are attributed to the remnant corrugated feature of the graphene sheets, as only a part of the diamond (111) planes is converted to graphite. Raising the HTT results in the increase of both intraplane and interplane ordering, signaling the formation of graphite phase at the expense of the diamond phase. This transformation is completed at 1600°C as can be seen from the HRTEM images and the x-ray diffraction pattern. However for this sample, $I_c = 0.353$ nm, still larger than that of bulk graphite ($I_c = 0.3345$ nm), and could be due to the turbostatic nature of the graphene planes. It is interesting to note that the intraplane diffraction from the graphene planes, namely, the (100) and (101) diffractions, are not observed in the HTT1200 sample. This indicates that the intrasheet ordering

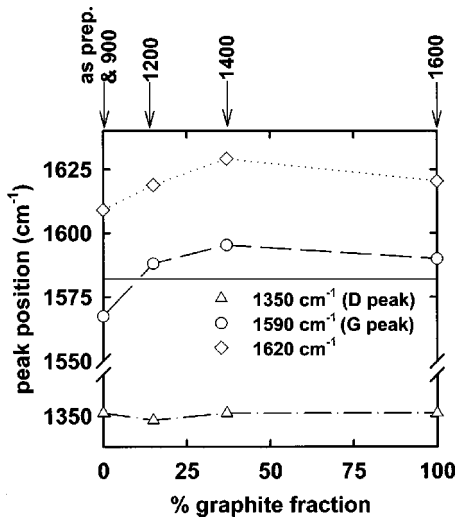


FIG. 8. The peak positions of Raman spectra as a function of the graphite fraction for 1350-cm^{-1} (*D*-peak), 1590-cm^{-1} (*G*-peak), and 1620-cm^{-1} regions. The solid line is the peak position for bulk-graphite *G* peak and the other lines are only guides for the eye. (The heat-treatment temperatures are also indicated at the top of the graph.)

in the HTT1200 sample may not be detectable by the x-ray diffraction due to the small sizes of the flat graphene planes. The HTT1400 sample shows some asymmetry in the peak around 43° , but the intensity was very low and hence the fitting was very difficult, while Raman spectra clearly depict the increase in the in-plane domain size for this sample. However, in the HTT1600 sample we could deconvolute the broad features into (100) and (101) peaks of graphite, and from the (100) peak width the in-plane size was estimated to be 3.6 nm. This is in good agreement with the Raman results and also consistent with ESR and magnetic susceptibility results, where dramatic changes are induced in the HTT1600 sample, while no such effects are observed in the HTT1200 and HTT1400 samples.

Important information on the electronic structure of these materials can be gained from the Raman peak positions, and they are plotted as a function of graphite fraction in Fig. 8.²³ The position of the *D* peak is almost constant, irrespective of the amount of graphite fraction present in the sample. However, the *G* peak and 1620-cm^{-1} peaks occur at different positions, depending on the graphite fraction. In samples with very low graphite fraction, the *G* peak is shifted downwards compared to the bulk-graphite value. In amorphous carbons it is generally observed that the increase in the sp^3 -bonded fraction would cause a downward shift in the position of the *G* peak.²⁴ This shift is assigned to the bond-angle disorder in these $sp^2:sp^3$ composite systems, where the tetrahedral sp^3 sites try to force the layers to be nonplanar while the sp^2 sites oppose the puckering of the layers. Theoretical models suggest that the *G* peak in disordered carbons shifts to higher wave numbers as the proportion of the sp^3 sites decreases,²⁵ and we indeed find an up shift in the *G*-peak position as the graphite fraction increases. In the case of samples with appreciable graphite fractions, the *G* peak is observed at higher wave numbers compared to bulk graphite. This can be tentatively explained in terms of the charge-transfer effect related to the edge states. As men-

tioned in Sec. I, recent theoretical reports suggest that the nonbonding π states from the edges appear as a flat band near the contact point of the $\pi-\pi^*$ levels of nanographite.^{5,6} They also pointed out that the charge density of these nonbonding π states are strongly localized on the edge sites. However, these calculations are performed assuming that the translational symmetry exists even in these nanometer scale materials, whereas the present samples are characterized with disordered structures inducing an energy level broadening. This would result in smearing of the band edges and consequently these bands may overlap, so that the bottom of the band from nonbonding edge states is lower than the top of the graphite π band. Thus it is possible that there is a charge transfer from the graphite π band to these nonbonding edge states where the edge states act as acceptors. This conjecture is justified by experimental evidence about the presence of holes in nanographites.²⁶ This is similar to graphite intercalation compounds (GIC's) with acceptors such as bromine.²⁷ In the case of bromine GIC's, the *G* band is found to shift to higher wave numbers as a result of charge transfer from the π band to the bromine atoms, which makes the bonds in graphene plane stiffer. If we consider charge transfer from the graphite π bands to the nonbonding edge states, this would also lead to stiffening of the C-C bonds in the plane, thus leading to the observed shift in the *G* band to higher wave numbers. It is reported that, in disordered carbons, the *G* peak is up-shifted in samples with small L_a 's and shifts downwards as the in-plane size increases above 10 nm.¹⁷ This supports our mechanism since as the in-plane size L_a increases, the edge states may have negligible role and hence no charge transfer. However, in the case of the $sp^2:sp^3$ mixed-phase systems, it would be difficult to exactly identify the origin of the *G*-peak shift as both these mechanisms, the bond-angle disorder due to the coexistence of $sp^2:sp^3$ carbons and the charge transfer to the edge states, will be competing with each other.

Here, on the basis of the above-mentioned structural characteristics, we broadly classify these materials into three groups, for the sake of clarity in discussing the electronic properties. Namely, samples dominated by sp^3 -bonded carbon (as-prepared nanoparticle diamond and the HTT900 sample with 0% graphite), the $sp^2:sp^3$ composite systems (samples HTT1200 and HTT1400 with 15% and 37% graphite), and the completely graphitized sp^2 -carbon-dominated system (HTT1600).

B. Electronic properties

The electronic properties of these materials are discussed below on the basis of ESR and magnetic susceptibility studies for the three broad classes mentioned above. As it will become clear, though the HTT1400 sample is grouped with the $sp^2:sp^3$ composite system, the π -electron network is more evidently developed here as compared with the HTT1200 sample.

The various parameters defining the electronic properties of these materials are plotted versus the graphite fraction in Fig. 9. We also provide in this figure [Fig. 9(c)] the orbital susceptibility for our samples, which corresponds to the susceptibility with the field parallel to the graphite *c* axis and is calculated by the equation

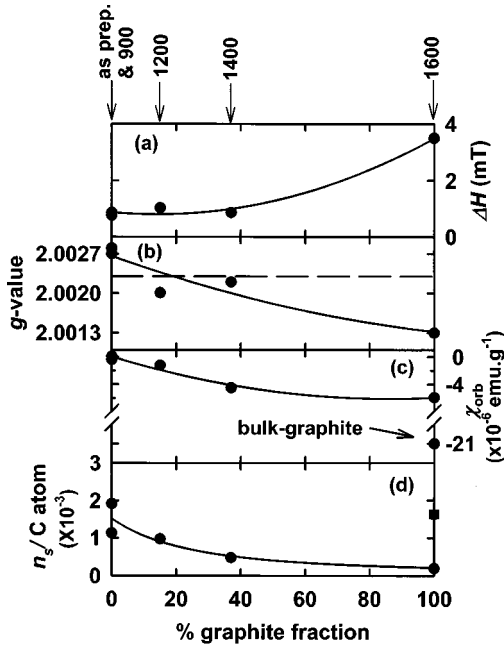


FIG. 9. (a) The ESR linewidths ΔH , (b) g values, (c) orbital susceptibility term χ_{orb} (see text for the details of calculation of χ_{orb}), and (d) localized spin concentration per carbon atom, n_s , as a function of graphite fraction. The dashed line in (b) represents the g value of free-electron spin. The full square at 100% graphite in (d) is the estimate of the π -electron concentration obtained from the Pauli susceptibility using the equation $k_B T \chi_P / \mu_B^2$, where χ_P is the Pauli susceptibility. Heat-treatment temperatures are indicated at the top of the graph. The solid lines are only guides for the eye.

$$\chi_{\text{orb}} = 3\chi_0 - 2\chi_{\perp},$$

where χ_0 is the susceptibility at infinite temperature with contributions from the orbital term, χ_{orb} , the Pauli paramagnetic term χ_P , and the core diamagnetic term χ_{core} . We assume that χ_{\perp} is equal to the core diamagnetism and is calculated from Pascal rules. We also assume that χ_P has negligible contribution to the observed susceptibility, which is justified by the fact that the χ_P from the π electrons is almost 10% even in the HTT1600 sample having the largest π -electron contribution. Here a comparison of the χ_{orb} of condensed polycyclic aromatic systems having N benzene rings, with the χ_{orb} observed for our samples might give important clues in understanding the development of π -electron structure of these materials as plotted in Fig. 10. The χ_{orb} for condensed polycyclic aromatic compounds was taken from the literature data²⁸ after doing necessary corrections for the anisotropy, like the one described above. We have considered the diamagnetic susceptibilities of highly symmetric molecules only (e.g., ovalene, ten benzene rings), since they show the maximum diamagnetic susceptibility compared with less symmetric molecules with same number of benzene rings. The straight line in the figure is a linear regression for the literature data. This plot also depicts the χ_{orb} of bulk graphite along with the χ_{orb} of our samples. The number of benzene rings for our samples were calculated from the Raman in-plane domain size using the equation

$$N \sim L_a^2 / S_0,$$

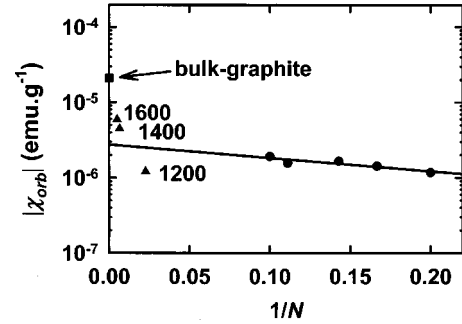


FIG. 10. The orbital susceptibility χ_{orb} of polycyclic aromatic molecules (full circles) compared with χ_{orb} of our samples (full triangles) and the χ_{orb} of bulk graphite (full square) plotted on a logarithmic scale vs $1/N$ (number of benzene rings, N). The numbers 1200, 1400, and 1600 denote the heat-treatment temperatures. The straight line is a linear regression for the data of aromatic molecules, which are taken from the literature (Ref. 28) after necessary corrections (see text for details).

where S_0 is the area of one benzene ring. For the samples with itinerant π electrons, the magnitude of χ_{orb} indicates the extent of delocalization of the π -electron network. It is clear from the figure that the observed χ_{orb} for our samples falls in two distinct regions of the straight line for the different graphite fractions. For the nongraphitized samples (as-prepared and HTT900), the observed χ_{orb} is almost negligible ($< 10^{-7}$ emu/g), suggesting the absence of an extended π -electron network. As the heat-treatment temperature increased (in other words, as the graphite fraction of the sample increases), the χ_{orb} gradually increases, suggesting the development of the graphite itinerant- π -electron system. Above 1400 °C $|\chi_{\text{orb}}|$ exceeds the value expected from the straight line for polycyclic aromatic rings and tends to approach the bulk-graphite value as the HTT increases. This suggests a steep development of the π -electron network in this HTT region. Below, we present a brief sketch of the sequence of the development of the nanographite π -electron network during the diamond-to-graphite conversion and correlate that to the structural transformations based on the experimental results.

The diamond nanoparticles are prepared by explosion-induced techniques in closed containers, resulting in the generation of high pressure in short time periods ($\sim \mu\text{sec}$).⁸ Due to this nonequilibrium condition in the formation of diamond, a large number of defects are produced as evidenced by the large spin concentration observed [Fig. 9(d)]. The observed g values of diamond nanoparticles are also quite close to the g values of microcrystalline diamond, where the spins are attributed to the paramagnetic centers created by the defects in the sp^3 -bonded network.²¹ As the HTT is raised to 900 °C, a lattice distortion, being in the equilibrium condition in the whole diamond particle, becomes relaxed in addition to the formation of disordered sp^2 carbon phase on the surface of the particle at the expense of the localized defect spins. This explains the large change in the spin concentration [Figs. 5(b) and 9(d)] from the as-prepared sample to HTT900 sample. On the other hand, the small χ_{orb} value and the negligible change in the g value at 900 °C suggest that the extent of itinerant- π -electron network is insignificant, and the localized spins in this sample are from the same

origin as that of the as-prepared sample. The absence of the graphite (002) x-ray diffraction peak and the similarity of HRTEM images of as-prepared and HTT900 samples also support these conclusions. Increasing the HTT to 1200 °C leads to severing of more and more diamond (111) planes from the diamond nucleus and converts them to graphite planes, as evidenced by the x-ray diffraction and HRTEM images. The observed ESR signal in this sample can be credited to the graphite π electrons, as the g value in these samples is less than that of free-electron spin value (g_0). As shown in Fig. 9(d), the localized spin density in this 15% graphitized sample is considerably lower than that of the 0% graphite samples, demonstrating that most of the localized spins are already becoming part of the extended π -electron network. However, the magnitude of the $|\chi_{\text{orb}}|$ is less than that expected on the basis of the number of benzene rings present (Fig. 10). This suggests that this sample is still dominated by defects (vacancies in the sp^2 network or remnant corrugated features from the diamond lattice) that effectively lead to a shrinkage in the graphite π -electron network. A further increment in the HTT to 1400 °C, while chipping more diamond (111) planes, makes the very small sp^2 -bonded fragments ordered into larger planar graphene sheets and this diamond-to-graphite transformation is complete at 1600 °C. For the more graphitized HTT1400 and HTT1600 samples, the $|\chi_{\text{orb}}|$ is more than that expected for polycyclic aromatic molecules with same number of benzene rings. In bulk graphite, the large enhancement of χ_{orb} compared to the value in large polycyclic aromatic molecules is attributed to the interband transitions,²⁹ since the π - π^* bands in bulk graphite are degenerate at the Fermi energy, whereas the aromatic molecules are characterized with an energy gap. Thus the increase in the χ_{orb} value from that expected on the basis of number of benzene rings clearly depicts the extended nature of the π -electron network. However, this value is still smaller than that of bulk graphite. We can attribute this feature to the finite crystallite sizes and also to the presence sp^3 -like defects in the case of the HTT1400 sample. Though the in-plane domain sizes are larger than that in the HTT1200 sample, the g value remains in the vicinity of g_0 and the ESR linewidths are small in the HTT1400 sample [Fig. 9(a) and 9(b)], indicative of the localized nature of the π -electron network to small regions due to the defects. Hence, it is concluded that in these sp^2 : sp^3 mixed-phase systems the itinerant π electrons from the graphite phase and the sp^3 defects from the diamond phase are homogeneously distributed over, and there is a possibility that these two spin species are strongly interacting with each other. In the case of the completely graphitized HTT1600 sample, the effect of the localized spins due to defects on the itinerant- π -electron network is quite insignificant because their absolute number is very low [Fig. 9(d)]. These localized spins are also associated with very few inhomogeneously distributed sp^3 -like defects, making them quite independent from the itinerant π electrons. Hence, at 1600 °C we see two different ESR signals unlike the HTT1200 and HTT1400 samples, where we see only one signal. In Fig. 9(d), we also provide the π -electron spin density obtained from the Pauli susceptibility¹¹ in the HTT1600 sample using the equation $k_B T \chi_P / \mu_B^2$, where k_B and μ_B are the Boltzmann constant and Bohr magneton, respectively. Here, it should be noted

that χ_P is governed mainly by the density of states of the nonbonding edge states.¹¹ It is quite clear from the figure that the localized spin density from defect origin is quite small ($\sim 10\%$) compared to the localized edge-state π -electron spin density. This implies that the presence of nonbonding edge states play a very important role in determining the electronic properties of the completely graphitized HTT1600 sample. More clearly, in the case of HTT1600, there might be a charge transfer from the graphite π band to the edge states shifting the Fermi level away¹¹ ($E_F \sim 0.1$ eV) from the π - π^* contact point, which is supported by the Raman peak shifts also. This leads to an apparent contraction of the π -orbital network, resulting in the reduction of the χ_{orb} value as observed here. The difference in g value at 1600 °C ($g = 2.0013$), from the g value of bulk graphite,³⁰ could also be explained by invoking the above charge-transfer mechanism. The g value observed in the HTT1600 sample is less than g_0 , while in bulk graphite, it is higher than g_0 . However, it is well known that the g value in bulk graphite is critically controlled by the location of the Fermi level and also by the ratio of holes and electrons present in the vicinity of the contact point of π and π^* bands.^{31,32} It is also reported that, in case of boronated pyrocarbons, a drastic drop in g value is observed, depending on the boron admixture in the pyrocarbons, which makes the Fermi level shift deeper into the valence band.³³ Thus the presence of Fermi level away from the contact point could explain the g -value deviation in the HTT1600 sample, though getting a quantitative estimation of the deviation is quite difficult.³²

Finally we would like to present a discussion about the change in spin-lattice relaxation processes observed. From the discussions presented earlier, we can summarize that the as-prepared diamond nanoparticles as well as the HTT900 sample are dominant sp^3 -bonded species, while the HTT1600 sample shows signs of well-developed π -electron network. Thus, the HTT1200 and HTT1400 samples seem to be sitting at the boundary of diamond-graphite phase transition. Here, we focus on the spin-lattice relaxation mechanism in relation to the development of the π -electron system, which substantially starts above 1200 °C. The spin-lattice relaxation time versus the heat-treatment temperature is plotted for the samples above a HTT of 1200 °C, which is obtained from the ESR saturation measurement, in Fig. 7. Here, for the HTT1600 sample, the broad signal ascribed to the π electrons is employed to determine the spin-lattice relaxation times. In the case of the HTT1600 sample, the spin-lattice relaxation time is governed by the interaction of conduction carriers with the nonbonding π electrons localized on the edge sites in addition to electron-particle boundary scattering.¹¹ This suggests that the particle edges working as fast relaxing centers are crucial to the spin-lattice relaxation process. We think the observed changes in the spin-lattice relaxation times as a function of HTT again originate from the contributions of these localized edge-inherited nonbonding π electrons. In case of the HTT1600 sample, where there is significant development of intraplane ordering the conduction electrons can easily come into contact with the nonbonding electrons of the edge origin, leading to faster relaxation times as observed. However, the HTT1200 sample is made up of very small graphitic islands well separated by defects, which originate from corrugated features from the remnant

buckling nature of the diamond lattice or vacancies in the graphite network due to partial conversion of diamond to graphite. These corrugated features of the graphene planes probably hinder the interaction of the electrons with fast relaxation centers at the edge. The HTT1400 sample is also featured with defects evident from the TEM, x-ray, ESR g -value and linewidth studies. However, the analysis of χ_{orb} (Fig. 10) reveals that there is appreciable development of the π -electron network compared to the 1200 °C heat-treated sample, though this sample is featured with sp^3 -like defects. The enhanced in-plane domain size from the Raman studies and the qualitative similarity of Raman spectra of this sample with the HTT1600 sample also supports this conclusion. Therefore it is possible that the itinerant π electrons are effectively relaxed by interacting with the edge-state electrons in this case also.

V. CONCLUSIONS

Heat-treatment-induced diamond-to-graphite conversion of diamond nanoparticles is investigated in relation to structural and electronic properties. When subjected to heat treatment below 1600 °C, the materials could be classified into three categories: the sp^3 -carbon-dominated diamondlike materials (as-prepared and HTT900 samples), $sp^2:sp^3$ mixed-phase systems (HTT1200 and HTT1400 samples), and the sp^2 -dominated complete graphitized system (HTT1600). In the initial stages of the heat treatment, the functional groups are stripped off from the diamond nanoparticle surfaces, resulting in a rearrangement of the sp^3 -bonded network [diamond (111) planes] into small localized sp^2 -bonded islands [graphite (002) planes]. As the heat-treatment temperature is increased (1200 and 1400 °C), first graphitic ordering is developed along the c axis, though the in-plane domain sizes are quite small. The larger c -axis repeat distance compared to the completely converted HTT1600 sample and bulk graphite indicates the remnant buckling feature of the diamond (111) planes at intermediate heat-treatment temperatures such as 1200 and 1400 °C. The orbital diamagnetism from the itinerant π electrons, which is negligible in the diamond nanoparticles and the HTT900 sample, starts contributing to the susceptibility from the HTT1200 sample onwards. Thus both structural and electronic properties show evidence for the development of a graphite π -electron network from HTT's of 1200 °C and up. However, due to the residual

puckered nature of the diamond (111) planes, the π -orbital network is localized to small regions. This is exemplified in the TEM, x-ray, Raman spectra, and orbital diamagnetism analyses. The graphitization process is complete at 1600 °C. The very low concentration of localized spins and their independent nature from the itinerant π electrons are indicative of the nearly complete conversion of the localized spins to itinerant π electrons during the graphitization process. In the completely graphitized sample there is a charge transfer from the graphite π band to the nonbonding states that originate in the edge, resulting in a stiffening of the intralayer vibration modes and a smaller orbital diamagnetism than expected, due to the shifting of E_F away from the π - π^* contact point. In the HTT1600 sample, the Pauli susceptibility is considerably enhanced compared to bulk graphite, due to the nonbonding states that originate in the edge, in agreement with the theoretical calculations.^{5,6}

The faster spin-lattice relaxation times observed in the case of more graphitized samples such as HTT1400 and HTT1600 samples are explained on the basis of interaction of the conduction carriers with the localized nonbonding π electrons working as fast-relaxation centers. The remnant nonplanar nature of the sp^3 -bonded carbon atoms in the more disordered HTT1200 sample obstructs such fast-relaxation processes.

In summary, heat treatment converts diamond nanoparticles to graphite nanoparticles from the particle surface inwards. The extent of itinerant graphite π -electron network gradually increases with heat-treatment temperature at the expense of localized defects. The charge transfer from the graphite π band to the nonbonding edge states and the resulting shift of the Fermi level crucially determine the electronic properties of these nanosized π -electron system.

ACKNOWLEDGMENTS

B.L.V.P. thanks the Japan Society for the Promotion of Science (JSPS) for a post doctoral financial support. The present work was supported by the Grand-in-Aid for "Research for the Future Program," Nano-carbons, from JSPS. A.M.R. and P.C.E. would also like to acknowledge financial support from the MRSEC NSF Grant No. DMR 9809686. The authors gratefully acknowledge many fruitful discussions with Professor Ko Sugihara and Professor Riichiro Saito.

*Author to whom correspondence should be addressed. Email: tenoki@chem.titech.ac.jp, Fax: +81-3-5734-2242.

[†]Present address: Department of Physics, Pennsylvania State University, 104 Davey Lab, University Park, PA 16802-6300.

¹R. Kubo, J. Phys. Soc. Jpn. **17**, 975 (1962).

²M. S. Dresselhaus, G. Dresselhaus, and P. C. Eklund, *Science of Fullerenes and Carbon Nanotubes* (Academic, San Diego, 1996).

³S. J. Tans, M. H. Devoret, H. Dai, A. Thess, R. E. Smalley, L. J. Geerligs, and C. Dekker, Nature (London) **386**, 474 (1997).

⁴J. W. G. Wildoer, L. C. Venema, A. G. Rinzler, R. E. Smalley, and C. Dekker, Nature (London) **391**, 59 (1998).

⁵M. Fujita, K. Wakabayashi, K. Nakada, and K. Kusakabe, J. Chem. Phys. **65**, 1920 (1996).

⁶K. Nakada, M. Fujita, G. Dresselhaus, and M. S. Dresselhaus, Phys. Rev. B **54**, 17 954 (1996).

⁷K. Wakabayashi, M. Fujita, H. Ajiki, and M. Sigrist, Phys. Rev. B **59**, 8271 (1999).

⁸V. L. Kuznetsov, A. L. Chuvilin, E. M. Moroz, V. N. Kolomiichuk, Sh. K. Shaikhutdinov, and Yu. V. Butenko, Carbon **32**, 873 (1994).

⁹K. C. Pandey, Phys. Rev. B **25**, 4338 (1982).

¹⁰G. Kern, J. Hafner, and G. Kresse, Surf. Sci. **366**, 445 (1996).

¹¹O. E. Andersson, B. L. V. Prasad, H. Sato, T. Enoki, Y. Hishiyama, Y. Kaburagi, M. Yoshikawa, and S. Bandow, Phys. Rev. B **58**, 16 387 (1998).

¹²T. Evans and P. F. James, Proc. R. Soc. London, Ser. A **277**, 260 (1964).

- ¹³A. E. Aleksenskii, M. V. Baidakova, A. Y. Vul, V. Y. Davydov, and Y. A. Pevtsova, *Fiz. Tverd. Tela (St. Petersburg)* **39**, 1125 (1997) [*Phys. Solid State* **39**, 1007 (1997)].
- ¹⁴E. D. Obraztsova, M. Fujii, S. Hayashi, V. L. Kuznetsov, Y. V. Butenko, and A. L. Chuvilin, *Carbon* **36**, 821 (1998).
- ¹⁵V. L. Kuznetsov, I. L. Zilberberg, Y. V. Butenko, A. L. Chuvilin, and B. Segall, *J. Appl. Phys.* **86**, 863 (1999).
- ¹⁶R. J. Nemanich and S. A. Solin, *Phys. Rev. B* **20**, 392 (1979).
- ¹⁷T. C. Chieu, M. S. Dresselhaus and M. Endo, *Phys. Rev. B* **26**, 5867 (1982).
- ¹⁸A. M. Rao, A. W. P. Fung, S. L. di Vittorio, M. S. Dresselhaus, G. Dresselhaus, M. Endo, K. Oshida, and T. Nakajima, *Phys. Rev. B* **45**, 6883 (1992).
- ¹⁹D. S. Knight and W. B. White, *J. Mater. Res.* **4**, 385 (1989).
- ²⁰A. S. Kotosonov, *Piz'ma Zh. Eksp. Teor. Fiz.*, **43**, 30 (1986) [*JETP Lett.* **43**, 38 (1986)].
- ²¹G. K. Walters and T. L. Estle, *J. Appl. Phys.* **32**, 1854 (1961).
- ²²L. S. Singer and J. Kommauder, *J. Chem. Phys.* **34**, 133 (1961).
- ²³M. S. Dresselhaus, G. Dresselhaus, M. A. Pimenta, and P. C. Eklund, *Analytical Applications of Raman Spectroscopy* (Chapman & Hall, London, 1998).
- ²⁴R. O. Dillon, J. A. Woolam, and V. Katkanant, *Phys. Rev. B* **29**, 3482 (1984).
- ²⁵D. Beeman, J. Silverman, R. Lynds, and M. R. Anderson, *Phys. Rev. B* **30**, 870 (1984).
- ²⁶Y. Shibayama, H. Sato, T. Enoki, X. X. Bi, M. S. Dresselhaus, and M. Endo, *J. Phys. Soc. Jpn.* **69**, 734 (2000).
- ²⁷M. S. Dresselhaus and G. Dresselhaus, *Adv. Phys.* **30**, 139 (1981).
- ²⁸H. Akamatsu and Y. Matsunaga, *Bull. Chem. Soc. Jpn.* **26**, 364 (1953).
- ²⁹B. T. Kelly, *Physics of Graphite* (Applied Science, London, 1981).
- ³⁰L. S. Singer and G. Wagoner, *J. Chem. Phys.* **37**, 1812 (1962).
- ³¹J. W. McClure and Y. Yafet, in *Proceedings of the 5th Conference on Carbon*, edited by S. Mrozowsky and P. L. Walker (Pergamon, Oxford, 1962), Vol. 1, p. 22.
- ³²K. Matsubara, T. Tsuzuku, and K. Sugihara, *Phys. Rev. B* **44**, 11 845 (1991).
- ³³A. S. Kotosonov, *Carbon* **26**, 735 (1988).